A single amino acid in RTEL1 determines telomere length in mice

Riham Smoom[1], Catherine Lee May[2], Vivian Ortiz[2,4], Mark Tigue[2], Hannah M. Kolev[2], Yitzhak Reizel[2], Ashleigh Morgan[2], Nachshon Egyes[1], Dan Lichtental[1], Emmanuel Skordalakes[3], Klaus H. Kaestner[2*] and Yehuda Tzfati[1*]

[1]Department of Genetics, The Silberman Institute of Life Sciences, Safra Campus, The Hebrew University of Jerusalem, Jerusalem, 91904, Israel

[2]Department of Genetics and Institute for Diabetes, Obesity and Metabolism, Perelman School of Medicine, University of Pennsylvania, Philadelphia, PA 19104, USA

[3]The Wistar Institute, Philadelphia, PA 19104, USA

[4]Division of Gastroenterology and Hepatology, Department of Medicine, Hospital of the University of Pennsylvania, Philadelphia, PA 19104, USA

[*]Correspondence: tzfati@mail.huji.ac.il (Y.T.) and kaestner@pennmedicine.upenn.edu (K.H.K.)

SUMMARY

Telomeres, the ends of eukaryotic chromosomes, protect genome integrity and regulate cell proliferation. Maintaining optimal telomere length in the germline and throughout life limits the risk of cancer and enables healthy aging. Telomeres in the house mouse, *Mus musculus*, are about five times longer than human telomeres, limiting the use of this common laboratory animal for studying telomere biology in aging and cancer. Here, we show that a single amino acid variation in the helicase 'Regulator of telomere elongation 1' (RTEL1), naturally occurring in the wild mouse *M. spretus*, is sufficient, when introduced into *M. musculus*, to alter the telomere length set point in the germline and generate mice with human-length telomeres. While these mice are fertile and healthy, the regenerative capacity of their liver is compromised. The engineered 'telomouse' reported here redefines the role of RTEL1 in telomere length regulation, and provides a unique model for aging and cancer.

KEYWORDS

telomeres, telomerase, helicase, RTEL1, aging, regeneration

INTRODUCTION

Telomeres maintain genome stability and enable cell proliferation by repressing the DNA damage response at the ends of linear chromosomes (de Lange, 2018). Human telomeres in most somatic cells shorten with each cell division due to incomplete replication and degradation (Roake and Artandi, 2020). In the germline, however, telomeres are elongated by the enzyme telomerase to compensate for the shortening and maintain them within a defined range referred to as "telomere length set point" (Boyle et al., 2020). The telomere length set point allows for sufficient, though not unlimited, cell divisions in the soma throughout life. Optimal age-appropriate telomere length is critical for maintaining genome stability and regulating cell proliferation and senescence, the major determinants of carcinogenesis and aging (Chakravarti et al., 2021; Lansdorp, 2022; Maciejowski and de Lange, 2017; Nassour et al., 2021; Rossiello et al., 2022). However, despite decades of research, it is not yet understood how telomere length homeostasis is achieved. The large difference (~ fivefold) in telomere length between two close and inter-breedable species of mice, *Mus musculus* and *M. spretus*, was exploited previously to search for genes that determine species-specific telomere length (Ding et al., 2004; Kim et al., 2003; Zhu et al., 1998). Interestingly, none of the known telomere maintenance genes were identified in these screens. Rather, the difference in telomere length between the two species was attributed to a single locus encoding a DNA helicase, which was therefore termed '*Regulator of Telomere Length'* (*Rtel1*)(Ding *et al.*, 2004; Zhu *et al.*, 1998). However, the difference between the *M. musculus* and *M. spretus* RTEL1 proteins that is responsible for the different telomere length set points has not been identified thus far (Lansdorp and van Wietmarschen, 2019).

RTEL1 belongs to a small family of iron-sulfur helicases together with XPD, FANCJ and ChlR1, which were implicated in the human inherited diseases Xeroderma pigmentosum, Fanconi anemia, and Warsaw breakage syndrome, respectively (van der Lelij et al., 2010; Wu et

al., 2009). Biallelic germline mutations in human *RTEL1* cause a fatal telomere biology disease named Hoyeraal-Hreidarsson syndrome (HHS) (Ballew et al., 2013a; Ballew et al., 2013b; Deng et al., 2013; Le Guen et al., 2013; Walne et al., 2013). HHS is characterized by accelerated telomere shortening and diverse clinical symptoms including bone marrow failure, immunodeficiency, and developmental defects (Glousker et al., 2015). Other HHS-causing mutations were found in telomerase subunits, or in factors essential for telomerase biogenesis or recruitment to telomeres (Grill and Nandakumar, 2021). While RTEL1 was reported to have multiple roles in maintaining the stability of the genome, and particularly the telomeres (Kotsantis et al., 2020; Porreca et al., 2018; Uringa et al., 2012; Vannier et al., 2012; Vannier et al., 2013; Wu et al., 2020), it was also suggested to regulate nuclear trafficking of ncRNA (Schertzer et al., 2015), the localization of telomeric repeat-containing RNA (TERRA) (Ghisays et al., 2021), and telomere elongation by telomerase (Awad et al., 2020; Uringa *et al.*, 2012).

One of the *RTEL1* missense mutations identified in HHS patients changes the highly conserved methionine 492 to isoleucine (Figure 1A,B) (Deng *et al.*, 2013). Methionine 492 is conserved nearly uniformly across vertebrates, with only a few species (mostly cats) having a leucine at this position. *M. spretus* is the only vertebrate species having a more radical change at this site, namely to the positively charged amino acid lysine (Deng *et al.*, 2013). We hypothesized that lysine 492 in *M. spretus* might be responsible for the difference in telomere length between the two mouse species (Deng *et al.*, 2013). Here we describe an engineered mouse that confirms this hypothesis and presents an invaluable model for the study of cancer and aging.

RESULTS

Methionine 492 is located at a critical position within the helicase core domain of RTEL1

Methionine 492 of RTEL1 is conserved in vertebrates but found to be altered in human HHS patients and in the short-telomere mouse species *M. spretus* (Deng *et al.*, 2013). To understand the role of this residue in RTEL1 function, we generated a structural model of the murine RTEL1 helicase domain using the software Protein Homology/analogY Recognition Engine V 2.0 (Phyre 2) (Kelley et al., 2015) and then modeled the complex with single-stranded DNA based on the X-ray crystal structure of the bacterial XPD family helicase DinG in complex with the DNA (Cheng and Wigley, 2018). This model revealed that methionine 492 (M492) is buried within the core of the helicase domain in proximity to the single-stranded DNA binding site of the protein, making extensive hydrophobic contacts with the hydrophobic side chains of residues M464, V468, F488, and I494 (Figure 1C,D) (Cheng and Wigley, 2018). Replacing methionine with the larger and positively charged lysine within this hydrophobic patch is predicted to perturb the local structure (Figure 1E), which in turn may affect the helicase DNA binding, translocation and unwinding activities of the protein.

A house mouse with short telomeres

To test if the lysine residue at position 492 of *M. spretus* is responsible for its shorter telomeres compared to the house mouse *M. musculus*, we generated a *M. musculus* strain in which methionine 492 was changed to a lysine (M492K) using CRISPR-Cas9 assisted genome editing in zygotes. We employed Nickase (D10A Cas9 mutant) mRNA and two guide RNAs to generate nicks on both strands of the *Rtel1* gene and facilitated gene conversion using a repair template (Figure 1F). Successful gene targeting in the resulting offspring was confirmed by DNA sequencing and by allele-specific Taqman probe-based PCR (Figure 1G,H). This founder mouse

was purified from potential off-target effects by backcrossing to wild-type (WT) C57BL/6 mice to generate F0 mice heterozygous for the *Rtel1*^{M492K} allele, termed *Rtel1*$^{M/K}$. F0 *Rtel1*$^{M/K}$ mice were intercrossed to generate F1 and F2 *Rtel1*$^{M/K}$. Homozygosity for the *Rtel1* mutation (*Rtel1*$^{K/K}$) was established in the third generation (F3). The homozygous *Rtel1*$^{K/K}$ mice were then bred *inter se* for eleven additional generations up to F14 to date, and were analyzed for telomere length and function as well as growth, fertility, and physiological parameters. We termed the *Rtel1*$^{K/K}$ mouse model 'telomouse'.

To determine the effect of the *Rtel1*^{M492K} mutation on telomere length, we employed two experimental paradigms. First, we established embryonic fibroblast cultures from *Rtel1*$^{M/K}$ and *Rtel1*$^{K/K}$ F3 embryos generated by intercrossing F2 *Rtel1*$^{M/K}$ mice. We also obtained WT (*Rtel1*$^{M/M}$) embryonic fibroblasts, generated from intercrossing WT mice. Mouse embryonic fibroblast (MEF) cultures were established by serial passaging and selection for spontaneous immortalization, and followed in culture over 250 population doublings (PD; Figure S1A-C). During the final growth phase, *Rtel1*$^{M/K}$, *Rtel1*$^{K/K}$ and *Rtel1*$^{M/M}$ MEFs grew at the same average rate (about one PD/day). We determined average telomere lengths at multiple time points by digesting high molecular weight genomic DNA with the restriction endonuclease *HinfI* and separating the restriction fragments by pulse-field gel electrophoresis (PFGE). Then, a telomeric C-rich probe was hybridized to the native DNA in the dried gel to estimate the average length of the G-rich single-stranded telomeric overhang (see below). Finally, the DNA was denatured and hybridized again to the same probe to detect both single- and double-stranded telomeric repeat tracts and estimate the length of the telomeric restriction fragments (TRF; representative gel images are shown in Figures 2A and S2-S4). The mean TRF length was repeatedly measured in different gels and PDs (Summarized in Supplementary Table 1 and Figure 2B). The average TRF in WT (*Rtel1*$^{M/M}$) MEFs was 46.9 kb at PD 10. It shortened slightly during the early growth

phase and stabilized at 38.4 kb through PD 250 (Figure 2A,B). In contrast, the mutant *Rtel1*$^{M/K}$ and *Rtel1*$^{K/K}$ MEFs displayed shorter telomeres at PD 10 (mean TRF length 34.2 and 30.1 kb, respectively), which continued to shorten gradually to 21.6 and 15.5 kb at PD 250, respectively (Figure 2A,B). Most (~55%) of the *Rtel1*$^{K/K}$ TRF at PD 250 were shorter than 20 kb (Figure 2C). Altogether, the average TRF length in the *Rtel1*$^{K/K}$ MEFs shortened by 60% as compared to the WT TRF length after 250 PD, and reached a length comparable to that of human fibroblasts immortalized by ectopic expression of telomerase (Vaziri and Benchimol, 1998).

RTEL1 dysfunction was proposed previously to cause telomere deletion and reduced telomerase action at telomeres by different mechanisms (Awad *et al.*, 2020; Uringa *et al.*, 2012; Vannier *et al.*, 2012). To distinguish the cause for telomere shortening in *Rtel1*$^{K/K}$ MEFs, we examined the distinct TRF banding pattern appearing in the *Rtel1*$^{M/K}$ and *Rtel1*$^{K/K}$ MEFs (Figures 2A, S2 and S3). Such banding pattern was observed previously in telomerase null MEFs (Blasco et al., 1997), as well as in mRtel1-deficient mouse embryonic stem cells (Uringa et al., 2012). It was suggested to represent homogenous telomere length of individual chromosomes within the cell population, which was fixed even in the presence of telomerase (Uringa *et al.*, 2012). Furthermore, this banding pattern showed gradual telomere shortening, indicating the inability of telomerase to elongate telomeres and compensate for the gradual shortening caused by the incomplete replication of the chromosome ends during cell divisions (Uringa et al., 2012). Based on this observation, the authors hypothesized that mRtel1 was required for the recruitment of telomerase to the telomeres. Similarly, *Rtel1*$^{M/K}$ and *Rtel1*$^{K/K}$ MEFs maintained several such sharp bands, which gradually shortened with continued passaging, indicating that telomerase activity was insufficient to maintain stable telomere length in these cells. The calculated rate of shortening after immortalization was 50-65 bp/PD for bands above 20 kb and slower for those shorter than 20 kb, suggesting that telomerase action was not lost but rather regulated to stabilize

telomeres on a new steady-state length. WT MEFs also displayed sharp bands during the initial growth phase, but these bands did not shorten but rather disappeared upon immortalization (Figures 2A, S2E,F and S3C,D), presumably due to the increased telomerase activity associated with immortalization of MEFs (Prowse and Greider, 1995). Thus, we conclude that the main reason for telomere shortening in the *Rtel1*$^{M/K}$ and *Rtel1*$^{K/K}$ MEF cultures is reduced telomerase action at chromosome ends.

We next noticed a significant decrease in the telomeric hybridization signal in samples of late PD with short telomeres (e.g., Figure 2A; K/K), and examined the correlation between the hybridization signal and mean TRF length. Since equal amounts of genomic DNA samples were loaded on the gels, we expected the denatured hybridization signal within each gel to correlate with telomere length – longer telomeres would bind more oligonucleotide probe and have stronger signals. Plotting mean TRF length as a function of the telomeric hybridization signal indeed revealed a linear correlation (Figure S5). Interestingly, however, the signal decreased faster than expected from the decrease of TRF length. Extrapolation of the regression line to zero signal suggested that the observed telomeric fragments are longer than the telomeric repeat tracks by an average of 10-15 kb. A plausible explanation is that they have long sub-telomeric sequences of low complexity that are underrepresented for *HinfI* restriction sites, contributing to the TRF length. Another possible explanation is that some telomeric fragments with short subtelomeres became too short to be detected by PFGE.

To directly compare the actual length of the telomeric repeat tracts between mouse and human telomeres, we applied mixed metaphase-arrested *Rtel1*$^{K/K}$ MEFs at PD 250 (mean TRF length 15 kb; Figure 2A,B) with human telomerase-positive fibroblasts (mean TRF length 14 kb; Figure 3D) to slides and hybridized them to telomeric (green) and centromeric (red) PNA probes (Figures 3A and S6). The centromeric probe enabled us to distinguish the human chromosomes,

which are mostly metacentric, from the acrocentric mouse chromosomes. The telomeric signals at each chromosome end were quantified using the *Telometer* plugin (available at https://demarzolab.pathology.jhmi.edu/telometer/index.html) of *NIH ImageJ* (Rasband, 1997-2014). The average telomeric signal intensity of the *Rtel1*$^{K/K}$ MEFs at PD 250 was comparable to that of the human telomeres (Figures 3A,C and S6), but significantly weaker than that of *Rtel1*$^{M/M}$ MEFs at PD 250 (Figure 3B,C), validating the PFGE results (Figure 2A,B). Interestingly, a significant portion of the telomeres displayed very weak hybridization signals, detectable only under much prolonged exposure (data not shown), indicating that they were extremely short but not completely lost (Figures 3 and S6). Moreover, regular (constant field) gel electrophoresis followed by in-gel hybridization revealed that a significant fraction of TRF in the *Rtel1*$^{K/K}$ MEFs PD 250 was shorter than 5 kb (Figure 3D). In sum, these data suggest that a significant fraction of *Rtel1*$^{K/K}$ MEFs telomeres is shorter than assessed by PFGE for two reasons: long subtelomeric regions included in the TRF observed by PFGE, and TRF that are too short to be detected by PFGE.

Finally, we employed long-read Nanopore sequencing of telomeres to obtain a precise length measurement of mouse telomeres. We adopted a STELA-based approach and ligated a telorette oligonucleotide with a C-rich six nucleotide telomeric repeat, which base pairs with the G-rich overhang (Sfeir et al., 2005), to the 5' end of the telomeres in undigested genomic DNA samples prepared from the *Rtel1*$^{K/K}$ and *Rtel1*$^{M/M}$ MEFs at PD 250 (Figure 4A). The other end of the double-stranded telorette oligonucleotide was designed to ligate to the Nanopore sequencing adaptor. We first used a mixture of equal amounts of telorettes of the six possible permutations (see Star Methods). As reported for human telomeres (Sfeir *et al.*, 2005), telorette 3 was the most frequently used (60 % of the *Rtel1*$^{M/M}$ and 76 % of the *Rtel1*$^{K/K}$ telomeric reads), indicating that the 5' strand of most telomeres ends in 3'-CCAATC-5' (Figure 4B). Therefore, for the rest of the

samples we used barcoded telorette 3 (see Star Methods). For long reads that begin with the telorette sequence on the 5' end of the sequenced C-rich strand and terminate with sub-telomeric sequences on the 3' end, we could determine the length of the telomere repeat sequences at base resolution. Telomeric sequencing reads were identified and processed computationally (examples for telomere reads are shown in Figure 4C; all telomeric reads are summarized in Supplementary Table 2). Notably, about 45% of the *Rtel1*$^{K/K}$ MEFs telomeres were shorter than 5 kb (Figure 4D), and thus likely not detected by our PFGE analysis. Using this precise methodology, we found that the average length of telomeric repeat tracks in *Rtel1*$^{K/K}$ MEFs is 6.86 kb. On the other hand, WT *Rtel1*$^{M/M}$ MEFs displayed an average telomere length of at least 27.2 kb, and likely more since a number of the nanopore reads did not reach the sub-telomeric region, and thus their full telomere length could not be determined (The incomplete reads are indicated in red in Figure 4D). Nanopore sequencing thus enables the determination of telomere length at base resolution and, most importantly, to identify and analyze the very short telomeres, which are not represented in the standard PFGE TRF analysis but are nevertheless of utmost importance in determining cell function and fate.

Functional telomeres in *Rtel1*$^{K/K}$ MEFs

The main function of telomeres is to suppress the DNA damage response (DDR) at chromosome ends, which can cause cell cycle arrest and deleterious fusions of chromosome ends (de Lange, 2018). The presence of DDR foci at telomeres, termed telomere dysfunction-induced foci (TIF), is a hallmark of telomere dysfunction. To examine if the telomeres of the *Rtel1*$^{K/K}$ MEFs retained their protective properties, we studied the presence of TIF using antibodies against the DDR marker γH2AX and the telomere protein TRF1 (Figure 2D). The overall levels of DDR were high in all MEF cultures, as reported previously for MEFs growing under atmospheric oxygen

levels (Di Micco et al., 2008). However, there was no significant difference in the number of DDR foci between the WT (M/M) and mutant (K/K) MEFs (Figure 2E). In addition, there was no increase in TIF formation in the mutant compared to WT MEFs (Figure 2F), indicating that even the short *Rtel1*$^{K/K}$ telomeres were functional and able to suppress the DDR as well as WT telomeres.

Shortened telomeric overhangs were found to be associated with telomere dysfunction in HHS patients and heterozygous carriers of the pathogenic M492I mutation in *RTEL1* (Awad *et al.*, 2020; Deng *et al.*, 2013; Lamm et al., 2009). To test whether the *Rtel1*^{M492K} mutation affected telomeric overhang maintenance in MEFs, we quantified the native in-gel hybridization signal as a measure of the average length of the G-rich single-stranded telomeric sequence. The native signal remained constant and comparable to that of WT fibroblasts (Figure S4). Thus, although the *Rtel1*^{M492K} mutation resulted in shorter telomeres, it did not compromise telomere function or the telomeric overhang, which is essential for the telomere end structure.

Short telomeres in *Rtel1*$^{K/K}$ mice

Telomeres of the *Rtel1*$^{K/K}$ MEFs shortened over time in culture, as described above. However, telomere shortening in cultured fibroblasts does not necessarily imply a reduced telomere length in the germline or in somatic tissues of mice. Therefore, we next analyzed telomere length in blood and tail DNA samples taken from *Rtel1*$^{K/K}$ mice over 10 generations (F4 to F13). In the blood, the mean TRF shortened at a constant rate of about 0.6 kb per generation, reaching an average of 23 kb in F13 *Rtel1*$^{K/K}$ mice as compared to 40 kb in the WT samples (Supplementary Table 3 and Figure 5A,C). In tail samples, TRF shortened with each generation, reaching an average of 21 kb in F13 *Rtel1*$^{K/K}$ mice as compared to 43 kb in the WT samples (Supplementary Table 3 and Figure 5B,D). Telomeres in the tail shortened faster in the early generations and

slower in the later generations, from 1.5 kb between F4 and F5 to 0.4 kb between F12 to F13 (Figure 5G). In comparison, telomeres of *M. musculus* deleted for telomerase RNA (*mTR*$^{-/-}$) shorten by 4.8 ± 2.4 kb per generation (Blasco *et al.*, 1997). These results indicate that telomerase activity was not completely eliminated in *Rtel1*$^{K/K}$ mice but only down regulated to reach a shorter telomere length set point with each successive generation. Notably, about 38% and 46% of the telomeric fragments in the F13 blood and tail, respectively, were shorter than 20 kb (Figure 5E,F). Consistent with the observation in MEFs, no reduction was observed in the native gel hybridization signal corresponding to the single-stranded G-rich telomeric sequences (Figures S7 and S8, for tail and blood samples, respectively), indicating that the *Rtel1*$^{K/K}$ mice maintained intact telomere end structures.

Decreased regeneration potential of *Rtel1*$^{K/K}$ liver hepatocytes *in vivo*

The *mTR*$^{-/-}$ telomerase null mice can be intercrossed for only six generations until fertility is lost (Blasco *et al.*, 1997). Cells from the fourth *mTR*$^{-/-}$ generation (G_4) onward frequently exhibit chromosome ends devoid of detectable telomere repeats, as well as end-to-end fusions and aneuploidy, correlating with defective spermatogenesis and reduced proliferation capacity of hematopoietic cells in the bone marrow and spleen (Lee et al., 1998). In contrast, as expected from the intact telomere end structure and function described above, *Rtel1*$^{K/K}$ mice showed normal morphology and proliferation rates in intestinal stem and progenitor cells, the fastest proliferating cells in the body (Figure 6A). EdU positive cells were found restricted to jejunal and colonic crypts in a pattern indistinguishable from WT mice. In the *Rtel1*$^{K/K}$ colon, we observed a small though nominally significant decrease in the EdU positive cells as compared to the WT.

While we did not observe any aberrant phenotypes in *Rtel1*$^{K/K}$ mice under normal homeostatic conditions, we suspected that a phenotype that distinguishes *Rtel1*$^{K/K}$ mice from control *Rtel1*$^{M/M}$ mice may appear when somatic cells are challenged in an extreme condition requiring rapid cell renewal of normally quiescent cells. Such a phenotype would indicate, as a proof of concept, that 'telomouse' can be used as a model for studying the effect of shorter telomeres on cell proliferation, cancer, and aging. To this end, we performed a competitive repopulation assay with normally quiescent adult hepatocytes. This assay takes advantage of the FAH (fumaryl acetoacetate hydrolase) null (*fah*$^{-/-}$) mouse model of conditional hepatocyte killing to drive massive expansion of transplanted hepatocytes (Grompe, 2017). Equal numbers of WT (GFP-positive) and *Rtel1*$^{K/K}$ (F10; GFP-negative) hepatocytes were transplanted into *fah*$^{-/-}$ mice and death of host hepatocytes was induced through withdrawal of the protective drug nitisinone (Figure 6B). The 50:50 mixture of the two genetically distinct hepatocytes was confirmed by TaqMan PCR genotyping (Figure 6C). In this model, transplanted quiescent hepatocytes reenter the cell cycle and replicate up to 12 times in order to restore functional liver mass. Four weeks after hepatocyte transplantation, livers were harvested and the proportion of FAH-expressing GFP^{+} and GFP^{-} hepatocyte repopulation nodules was quantified. Figure 6D shows a representative section of the liver, where repopulation nodules are marked in red (indicating transplanted *FAH* cells). In addition to red, WT hepatocyte nodules are marked in green. Quantifying the fraction of hepatocyte nodules by genotype over multiple liver sections, we observed a significant decrease in the number of repopulation nodules derived from *Rtel1*$^{K/K}$ hepatocytes, as compared with the WT hepatocytes (Figure 6E). These data demonstrate a significant impairment in the induced proliferative capacity of *Rtel1*$^{K/K}$ hepatocytes with shortened telomeres. Interestingly, the average size of the *Rtel1*$^{K/K}$ nodules was not different from the *Rtel1*$^{M/M}$ nodules (Figure 6F), indicating that *Rtel1*$^{K/K}$ hepatocytes were compromised in

the first phase of initiation of a new nodule, but not in the later ability to proliferate once the nodule had been established.

DISCUSSION

RTEL1 was reported 18 years ago as a regulator of telomere elongation, based on its genetic association with telomere length in crosses between the long-telomere species *M. musculus* and the closely related, short-telomere species *M. spretus* (Ding *et al.*, 2004). However, the functional difference between the RTEL1 proteins from the two mouse species that is responsible for the different telomere lengths has remained unknown to date (Lansdorp and van Wietmarschen, 2019). We derived a novel strain of *M. musculus* with a point mutation in *Rtel1*, replacing methionine 492 with a lysine, which we termed 'telomouse' (Figure 1). Following the growth of MEFs derived from the $Rtel1^{K/K}$ mice over 250 population doublings and analyzing their telomeres by PFGE revealed that they gradually shortened to a mean TRF length of 15.5 kb (Figure 2). However, more careful analysis of the PFGE results and qFISH hybridization signal, and precise measurement of individual telomeres by Nanopore sequencing revealed high length heterogeneity in the telomeres of the $Rtel1^{K/K}$ MEFs PD 250, with a significant number of telomeres being shorter than five kb and a mean telomere length of 6.86 kb (Figures 3,4). Nevertheless, even the short telomeres retained their end-protection function, as observed by TIF formation, which was comparable to the WT (Figure 2D,F). Interestingly, heterozygous $Rtel1^{M/K}$ MEFs displayed telomeres nearly as short as the homozygous $Rtel1^{K/K}$ MEFs (Figure 2A,B), suggesting that the $Rtel1^{M492K}$ mutation is dominant in determining telomere length.

Interbreeding $Rtel1^{K/K}$ mice over eleven generations revealed that in each generation telomeres shortened, suggesting a comparable reduction of the telomere length set point in the germline. The observed rate of shortening (1.5 to 0.4 kb per generation in tail, and 0.6 kb per

generation in blood) is much slower than the rate of shortening in the telomerase null (*mTR*$^{-/-}$) mouse (4.8 kb per generation) (Blasco *et al.*, 1997). This indicates that telomerase action was not completely lost in the *Rtel1*$^{K/K}$ mice, but rather down-regulated to achieve a shorter telomere length set point. Together, our results confirm that the M492K mutation altered the function of RTEL1 in telomere length regulation, in line with other reports suggesting that RTEL1 regulates telomerase action at telomere ends (Awad *et al.*, 2020; Deng *et al.*, 2013; Ding *et al.*, 2004; Porreca *et al.*, 2018; Uringa *et al.*, 2012). Importantly, the M492K mutation only affected telomere length but not genome stability or telomere function, unlike the disease-causing mutation (M492I) in human cells, indicating a separation of function between these two mutations at the same position, and suggesting that RTEL1 regulates the accessibility or processivity of telomerase at the telomeric 3' overhang.

To enable precise, base-resolution measurements of telomere length, we developed a novel method for telomere length analysis by long read Nanopore sequencing. This technique provides the mean, distribution and, most importantly, length and percentage of the shortest telomeres, the latter of which cannot be determined by Southern blot or by in-gel hybridization analysis. This is particularly important, because the shortest telomeres are those which dictate cell function and fate (Hemann et al., 2001). In addition, Nanopore sequencing can identify and assign individual chromosome ends. In sum, the Nanopore sequencing technique revealed that not only the telomeres of the 'telomouse' are shorter on average than those of WT *M. musculus* mice, but they also include very short telomeres not observed by other methods..

Short telomeres are major drivers of the aging-dependent decline in organ function and increase in cancer risk (Hanahan, 2022; Lansdorp, 2022). Unfortunately, to date, these processes have been difficult to study in the common laboratory mouse, *M. musculus,* due to its extremely long telomeres. Attempts to study the implications of short telomeres in mice have thus far been

based on telomerase null alleles, which cause ever-shortening telomeres and eventually result in severe pathologies and infertility, or on manipulating telomere proteins to induce overt telomere deprotection (Chakravarti *et al.*, 2021; Li et al., 2019). These existing mouse models are limited by their inability to maintain short but stable telomeres with function and lengths comparable to those of humans. The *Rtel1*^{M492K} 'telomouse' model is genetically identical to the common laboratory strain C57BL/6, except for the single amino acid difference in RTEL1. Yet, it displays dramatically shorter telomeres with no signs of telomere dysfunction under normal physiological conditions, even in the fastest proliferating cells of the intestine, and no decline in fertility. However, when normally quiescent hepatocytes were forced to reenter the cell cycle and replicate multiple times to regenerate the damaged liver, *Rtel1*$^{K/K}$ hepatocytes were found to be compromised in their ability to generate new liver nodules. The average size of the *Rtel1*$^{K/K}$ nodules was not different from that of the WT, suggesting that the *Rtel1*$^{K/K}$ hepatocytes were impaired in the initial phase of reentering the cell cycle and establishing a regenerative nodule, rather than in cell proliferation itself. How very shorter telomeres might compromise the transition of G0 hepatocytes to a proliferative stage remains to be explored. In the future, this model will allow additional studies on the mechanism of cancer transformation, particularly liver and hematopoietic malignancies (Kirwan et al., 2009), as well as telomere biology disorders and other pathologies correlated with telomeres and aging, such as idiopathic pulmonary fibrosis (Armanios et al., 2007; Duckworth et al., 2021), non-cirrhotic portal hypertension, aplastic anemia (Al-Rahawan et al., 2006), and diabetes (Cheng et al., 2022). In sum, the 'telomouse' model promises to reveal the effects of short telomeres in various tissues on cell proliferation, age-related organ decay, and cancer development.

ACKNOWLEDGEMENTS

This research was supported in parts by the Israel Science Foundation grant 2071/18 to Y.T., the NIDDK through R37-DK053839 and R01-CA249929 to K.H.K., and by the Israel-UK-Palestine GROWTH Fellowship to R.S.

We are grateful to all members of the Tzfati and Kaestner laboratories for stimulating discussions and assistance. We thank Ittai Ben-Porath and Amir Eden for the gifts of WT mice and MEFs, Devora Olam for assistance in mouse blood collection, Naomi Melamed-Book, Bio-Imaging Unit at the Hebrew University, for assistance with confocal imaging, and Manish Goyal for assistance with super-resolution microscopic imaging, Dana Avrahami-Tzfati for assistance with CRISPR, and Ran Avrahami for assistance with statistical analyses. We thank the University of Pennsylvania's Diabetes Research Center (DRC) for the use of the Functional Genomics Core (P30-DK019525) and the Center for Molecular Studies in Digestive and Liver Diseases for the use of the Molecular Pathology and Imaging and Transgenic and Chimeric Mouse Cores (P30-DK050306). We also thank Lan Cheng in IDOM Histology Service for performing the IF staining, and Ayano Kondo for writing a code for *ImageJ* analysis.

AUTHOR CONTRIBUTIONS

Corresponding authors Y.T. (telomere biology) and K.H.K. (mouse biology): study concept and design; analysis and interpretation of data; writing and revising the manuscript. Y.T. R.S.: study concept and design; analysis of telomere phenotypes; interpretation of data; writing and revising the manuscript. C.L.M. and H.K.: derivation and *in vivo* analysis of the mouse strains, and writing and revising the manuscript. N.E.: analysis of telomere phenotypes. D.L.: computational analysis of Nanopore sequencing data. E.S.: computational analysis of the mouse RTEL1 structure. Y.R., A.M., V.O. and M.T.: *in vivo* analysis of the mouse strains.

DECLARATION OF INTERESTS

The authors declare no competing interests.

FIGURE LEGENDS

Figure 1. The RTEL1 helicase domain. (A) A map delineating the domains of RTEL1. The N-terminal part of the protein includes helicase domains 1 and 2 (HD1 and HD2), the iron-sulfur coordinating cluster (FeS) and the ARCH domain. The C-terminal part includes the nuclear localization signal (NLS), two harmonin N-like domains (HNL1 and HNL2), the PCNA interacting protein motif (PIP), and a C4C4 ring-finger domain. (B) Protein sequence alignment showing position 492 with a conserved methionine in *M. musculus* and human (mutated to isoleucine in HHS), and a lysine in *M. spretus.* (C) Predicted structure model of the *M. musculus* RTEL1 helicase domain, formed by residues 3-777 of mRTEL1 in a complex with the single-stranded DNA. (D) Enlargement of the helicase domain in the black box in (C), showing the contacts of M492 with several hydrophobic residues and distances in Å. (E) Replacing M492 with the larger and charged lysine and overlaying the energy-minimized WT (green) and mutant (light brown) structures reveals changes in the position of nearby residues, which may affect the interaction with the adjacent single-stranded DNA. (F) Derivation of an Rtel1^{M492K} allele using the CRISPR-Cas9 Nickase editing strategy. Illustration showing WT allele, two gRNAs targeted positions (blue and red arrowheads), ssDNA repair template with the mutation, left homology arm (blue), right homology arm (red) and the resulting targeted allele. (G) Sanger sequencing of founder #15 confirming the replacement of the “T” with an “A” at the codon encoding methionine 492, changing it to a lysine (underlined). (H) Genotyping of animals using Custom Taqman SNP Genotyping Assays. WT (M/M; blue), heterozygotes (M/K; green), homozygotes (K/K; red), and no-template control (NTC; yellow).

Figure 2. Telomeres of MEFs carrying the *Rtel1*^{M492K} mutation progressively shorten with cell division in culture. (A) Genomic DNA samples prepared from WT (M/M), or mutant homozygous (K/K) or heterozygous (M/K) *Rtel1*^{M492K} MEF cultures were analyzed by PFGE and in-gel hybridization to the denatured DNA. Mean telomere length (indicated below the lanes) was quantified by *TeloTool* (Gohring et al., 2014). (B) Mean TRF length for each of the sampled PD were repeatedly measured in additional gels (summarized in Supplementary Table 1) and plotted. (C) The percentage of telomeric fragments shorter than 20 kb for each sample was calculated from the mean and standard deviation of TRF lengths obtained by *TeloTool* (Supplementary Table 1). (D) The formation of DDR foci and their localization to telomeres (defined as TIF) were evaluated by immunofluorescence with antibodies detecting the DDR marker γH2AX (red) and the telomere protein TRF1 (green). Scatter plots show the number of DDR foci (E) and TIF (F) per nucleus (127 and 111 nuclei counted for M/M and K/K, respectively). The mean values are indicated by black lines. The P values calculated by nested t-test were 0.16 and 0.26 for DDR and TIF, respectively.

Figure 3. FISH reveals that *Rtel1*$^{K/K}$ MEFs telomeres are comparable in average length but more heterogeneous than human telomeres. (A) *Rtel1*$^{K/K}$ MEFs PD 250 and human fibroblasts with mean TRF length of 14 kb (as measured by in-gel hybridization, see (D)) were arrested in metaphase, mixed and spread on slides. The slides were hybridized to a green telomeric PNA probe and a red centromeric probe to distinguish the human mostly metacentric chromosomes from the mouse acrocentric chromosomes. (B) *Rtel1*$^{M/M}$ MEFs were processed in the same conditions and hybridized as in (A). (C) The telomeric signals were quantified using the *Telometer* plugin of *NIH ImageJ*. Violin plots show the distribution of individual telomeric

signal intensities in seven pairs of human and mouse *Rtel1*$^{K/K}$ metaphase cells (1-7) and three mouse *Rtel1*$^{M/M}$ metaphase MEFs (8-10). Horizontal lines indicate quartiles. (D) Genomic DNA was extracted from the same cultures shown in (A) and (B) and analyzed by regular gel electrophoresis and in-gel hybridization to the denatured DNA.

Figure 4. Long-read Nanopore sequencing reveals large heterogeneity and short telomeres in the mouse telomeres. (A) A scheme showing the ligation of a telorette oligonucleotide complementary to the G-rich telomeric overhang to the 5' end of the telomere, followed by the ligation of the Nanopore sequencing adaptor. (B) High molecular weight genomic DNA prepared from *Rtel1*$^{K/K}$ or *Rtel1*$^{M/M}$ MEFs PD 250 was ligated to a mixture of equal amounts of six telorette oligonucleotides, each ending with a different permutation of the C-rich 6 nucleotide telomeric repeat, and then ligated to the nanopore sequencing adaptor and sequenced. The bar graph shows the percent of the telomeric reads ligated with each telorette. (C) The reads were identified and processed computationally, and presented in graphs of telomeric repeat density (the portion of telomeric repeats, from 0 to 1, within a moving window of 50 nucleotides).

Indicated are the precise telomere length and read length. Two representative examples are shown and the other reads are summarized in Supplementary Table 2. (D) Violin plots show telomere lengths of individual reads of the indicated MEFs and mouse tail and blood samples, with median (in red) and quartiles (in black) horizontal lines. Red circles indicate incomplete telomere reads in which sequencing did not reach the sub-telomeric region.

Figure 5. Telomeres of mice carrying the *Rtel1*^{M492K} mutation progressively shorten over generations. Genomic DNA samples extracted from blood leukocytes (A) or tail (B) from mutant (K/K) or WT (M/M) mice at the indicated generations and ages were analyzed by PFGE

and in-gel hybridization to the denatured DNA. Representative gels are shown. Mean TRF length for each generation was repeatedly measured from (C) blood (n= 31 for M/M and 64 for K/K) and (D) tail (n= 33 for M/M and 129 for K/K) samples in additional gels and plotted. Rates of telomere shortening per generation were calculated from the best-fit regression lines [2nd order polynomial (Y=37.62-2.159*X+0.06853*X^2) for tail and linear (Y=-0.6069*X+31.09) for blood]. (E,F) The percentage of telomeric fragments shorter than 20 kb for each sample was calculated from the mean and standard deviation of TRF lengths obtained by *TeloTool.* All data are summarized in Supplementary Table 3.

Figure 6. Intestinal tissues display normal histology and proliferation rates, but liver regeneration is impaired in *Rtel*$^{K/K}$ mice. (A) Intestinal tissues from *Rtel1*$^{K/K}$ mice (F13) were analyzed for the homeostatic proliferation rate in the gut epithelium by short-term (120 minutes) EdU labeling. Crypt stem and progenitor cells in the jejunum of mutant (K/K) mice displayed proliferation rates similar to those observed in WT (M/M) mice, but in the colon the mutant cells divided somewhat less frequently. N=4. (B) Scheme for the competitive hepatocyte repopulation study. WT (M/M) GFP-positive hepatocytes and mutant (F10 K/K) GFP-negative hepatocytes were mixed in a 1:1 ratio and transplanted into FAH null mice. After removal of the protective drug, nitisinone, host hepatocytes died and transplanted G0 hepatocytes were forced to re-enter the cell cycle and proliferate rapidly. Outcome 1 illustrates both types of hepatocytes having equal repopulation capacity, and outcome 2 an advantage of WT hepatocytes over the *Rtel1* mutants. (C) TaqMan assay of the mixed hepatocytes confirms equal numbers of each genotype among the transplanted cells. (D) A representative liver section stained for FAH protein (red) to label all repopulation nodules, while GFP (green) labels only the repopulating WT hepatocytes. White arrows indicate GFP-negative repopulation nodules from the K/K mutant donor mouse.

Note that the WT (green) hepatocyte nodules are overrepresented. (E) GFP-negative hepatocytes from K/K mutant F10 mice displayed an average of 39% reduction in the number of repopulation nodules compared to simultaneously transplanted GFP-positive WT hepatocytes. N=5. (p value = 0.0022 by paired t-test). The graph shows the mean with SEM. (F) The area occupied by 23-27 FAH positive nodules was quantified by *NIH ImageJ* (Rasband, 1997-2014) from two different regions of each mouse from three experiments. No significant difference was detected between M/M and K/K nodules area calculated by nested t-test (two-tailed p value = 0.95).

STAR METHODS

Generating a three-dimensional structure model of the murine RTEL1 helicase domain

We generated the murine RTEL1 (mRTEL1) 3D structure model consisting of residues 3-770 using the software Protein Homology/analogY Recognition Engine V 2.0 (Phyre 2), which produces a model of the protein of interest based on sequence alignment to known structures (Kelley *et al.*, 2015). The 3D mRTEL1 structure was modeled based on the cryo-EM structure of the yeast TFIIH helicase in the contracted state within the pre-initiation complex (PDB ID: 7O4K) (Schilbach et al., 2021). TFIIH has 28% sequence identity to the mRTEL1 helicase domain. The presence of a structure with significant sequence identity with the murine gene enabled PHYRE to generate this model with 100% confidence. The model was further refined by applying geometry minimization in UCSF CHIMERA (Pettersen et al., 2004). We then generated a model of RTEL1 in complex with single stranded DNA, using the complex structure of the highly similar helicase domain of DinG (PDB ID: 6FWS), which belongs to the XPD family of helicases together with RTEL1, FANCJ and DDX11. The model was further refined by applying geometry minimization in Phenix (Afonine et al., 2010). The figures were generated in Pymol (LLC).

Derivation of Rtel1^{M492K} mice

CRISPR guide RNAs were designed as described (Yang et al., 2014). For sgRNA preparation, the T7 promoter sequence was added to the sgRNA template by PCR amplification using pX335 (Addgene #42335) with Phusion high-fidelity DNA Polymerase Kit (NEB), Common primer and Primer 1 or Primer 2 (see below).

Common sgRNA-R: `5'-AGCACCGACTCGGTGCCACT-3'`

Primer 1 with gRNA sequence underlined:

`5'-TTAATACGACTCACTATAGG`**`CATCTGCATCTCCAGAGCAA`**`gttttagagctagaaatagc-3'`

Primer 2 with gRNA sequence underlined:

`5'-TTAATACGACTCACTATAGG`**`CACCTGGAGGTCACAACACT`**`gttttagagctagaaatagc-3'`

PCR products were purified using QIAquick Gel Extraction kit (Qiagen), followed by in vitro transcription using T7 High Yield RNA Synthesis kit (NEB). Newly synthesized sgRNAs were purified using the MEGAclear kit (Life Technologies), precipitated and diluted in injection buffer (10 mM Tris / 0.1 mM EDTA, pH 7.5) at a concentration of 500 ng/µl. The quality of the sgRNAs was bioanalyzed using the total RNA Nano Chip. Final injection mix was prepared using ssDNA repair template (IDT; 100 ng/µl), sgRNA1 (50 ng/µl), sgRNA2 (50 ng/µl), and Cas9 Nickase mRNA (Trilink; 100 ng/µl) in injection buffer. The sequence of the ssDNA repair template is shown below. The mutated A is underlined within codon 492 in bold.

`5'-GTTCGTACCCTTATCCTCACCAGCGGTACCCTGGCTCCACTGTCTTCCTTTGCTCTGGAG`**`AAG`**`CAGA`
`TGTATGTATGAGTCACCTGGAGGTCACAACACTAGGAACATGGTGGGTGGGGTTGG-3'`

The final mix was spun twice at top speed for 30 minutes at 4˚C to remove debris to avoid needle clogging. Cytoplasmic injection was done using C57Bl6 zygotes. After injection, SCR7 (Xcessbio) was added to the overnight egg culture at the concentration of 50 µM. Out of the 17 mice born, two had the targeted allele.

Preparation of and culture of MEF

Embryonic day (E)13.5 mouse embryos were dissected with head and inner organs removed, rinsed in HBSS, then digested with 300µl papain isolation enzyme (ThermoFisher) for 30 minutes at 37˚C following manufacturer's protocol. In brief, embryonic digests were transferred to conical tubes with 1ml of HBSS, pipetted up and down to achieve single cell suspension and then spun. The pellets were re-suspended in MEF media (DMEM with 10% FCS, Pen/Strep/non essential amino acids) and plated. MEFs were grown in DMEM media containing 2 mM L-glutamine, penicillin-streptomycin, non-essential amino acids and 20% fetal bovine serum until immortalization (around PD60-70) and then 10%. Media and media supplements were purchased from Biological Industries Inc., Beit Haemek, Israel.

Genomic DNA extraction

Leukocytes were obtained from blood by lysing red blood cells in 155 mM NH_4Cl, 10 mM $KHCO_3$ and 0.1 mM EDTA pH 8 and precipitation. Leukocytes and MEFs were lysed in 10 mM Tris pH 7.5, 10 mM EDTA, 0.15 M NaCl, 0.5% SDS and 100 µg/ml proteinase K overnight at 37˚C. Mouse tail samples were lysed in 100 mM Tris HCl pH 8.5, 5 mM EDTA, 0.1% SDS, 200 mM NaCl and 100 µg/ml proteinase K overnight at 50˚C. Following cell lysis, high molecular weight genomic DNA was phenol-extracted, ethanol-precipitated, and dissolved in TE.

In-gel analysis of telomeric restriction fragments

Genomic DNA was treated with RNase A, digested with *HinfI* restriction endonuclease, and quantified by Qubit fluorometer. Equal amounts (3-5 µg) within each gel of the digested DNA samples were separated by pulsed-field gel electrophoresis (PFGE) using a Bio-Rad CHEF DR-II apparatus in 1% agarose and 0.5 x TBE, at 14˚C, 200V and pulse frequency gradient of 1 sec

(initial) to 6 sec (final) for 22 hr (except for the K/K gel on the right in Figure 2A, which was electrophoresed in the same parameters but for 18 hr), or in regular gel apparatus, 0.7% agarose and 1 x TBE for 1,300 V x hr. Gels were ethidium-stained, dried and hybridized as previously described (Awad *et al.*, 2020). Probe mixtures contained a telomeric oligonucleotide $(AACCCT)_3$, and mid range PFG ladder (NEB Inc.) and 1 kb ladder (GeneDirex Inc.), which were digested with *HinfI*, dephosphorylated by quick calf intestinal phosphatase (NEB Inc.) and heat-inactivated. All probes were 5' end-labeled with [alpha-^{32}P]-ATP and T4 polynucleotide kinase (NEB Inc.). The gels were exposed to a PhosphorImager. TRF length was quantified using *TeloTool* (corrected mode) (Gohring *et al.*, 2014). Individual band length was interpolated from regression formulas of the ladder bands size per migration distance, and native and denatured in-gel hybridization intensity was quantified using *ImageQuant-TL* (GE Healthcare Inc.).

Immunofluorescence of cultured cells

Cells were seeded onto glass coverslips and grown for 1-4 days. Immunofluorescence was performed as described (Gohring *et al.*, 2014) with the following changes: Primary antibodies used were TRF1 (Abcam; AB10579) and γH2AX (Cell Signaling Technology; 2577S), incubated overnight at 4˚C. Imaging acquisition was by FV-1200 confocal microscope (Olympus, Japan) with a 60X/1.42 oil immersion objective. *NIH ImageJ* (Rasband, 1997-2014) was used for image analysis and foci quantification.

Metaphase FISH

Metaphase spread and FISH were performed as described (Awad *et al.*, 2020). Cells were arrested in metaphase by 3-4 hr incubation with colcemid. After fixation, both MEFs and human

fibroblasts were mixed and dropped on the slides. The PNA probes used were TelC-Alexa488 telomeric probe (F1004, Panagene Inc.) and CENPB-Cy3 centromeric probe (F3002, Panagene, Inc). Imaging acquisition was by FV-1200 confocal microscope (Olympus, Japan) or by a Nikon Eclipse Ti-E super-resolution microscope equipped with a CoolSNAP Myo CCD camera. Telomeric signal was quantified using *Telometer* following the manual (van Batenburg et al., 2018).

Nanopore sequencing of telomeres:

For the K/K and M/M MEFs PD250 (Figure 4), each separate sequencing reaction included 10µg of high molecular weight genomic DNA, prepared as described above, treated with RNase A, and ligated at 20˚C overnight with a mix of six 5' phosphorylated telorette oligonucleotides (0.1µM each) and 2,000 units of T4 ligase (NEB Inc.) in a 50µl reaction. The ligated DNA was then annealed to Teltail-tether oligonucleotide by adding 1µM of Teltail-tether, heating for 10 minutes at 65˚C and cooling slowly to room temperature. The DNA was purified using AMPure XP beads (Beckman Coulter Life Sciences), and ligated to the Nanopore sequencing adapter (AMII) following the protocol for genomic DNA ligation sequencing with native barcoding (SQK-LSK109 with EXP-NBD104; Oxford Nanopore Technologies). The M/M MEFs PD110 and the mouse tail and blood samples (Figure 4) were combined in the same sequencing reaction using barcodes, as follows: Each barcoded telorette 3 (Telorette3-NB01, Telorette3-NB02 and Telorette3-NB03) was first annealed to Teltail-tether and then ligated to a different DNA sample in a reaction containing 3 µg genomic DNA and 1 µM annealed telorette as described above. The reaction was stopped by adding 20 µM EDTA and the three barcoded samples were combined, purified by polyethylene glycol (PEG) precipitation, ligated to the sequencing adaptors (3 µl AMII) using NEB-NEXT quick ligase, and purified again by PEG precipitation following

(Tyson, 2020). Sequencing libraries were loaded onto the Nanopore R9 flow cell with SQB buffer (Oxford Nanopore Technologies) without loading beads due to the high viscosity of the library.

Oligonucleotides (underlined are the permutated telomeric sequences; P, 5' phosphate):

Telorette1: 5'-P-TGCTCCGTGCATCTCCAAGGTTCCTAAC-3'

Telorette2: 5'-P-TGCTCCGTGCATCTCCAAGGTTAACCCT-3'

Telorette3: 5'-P-TGCTCCGTGCATCTCCAAGGTTCTAACC-3'

Telorette4: 5'-P-TGCTCCGTGCATCTCCAAGGTTTAACCC-3'

Telorette5: 5'-P-TGCTCCGTGCATCTCCAAGGTTACCCTA-3'

Telorette6: 5'-P-TGCTCCGTGCATCTCCAAGGTTCCCTAA-3'

Telorette3-NB01:
5'-P-TGCTCCGTGCATCTCC-AAGGTT-CACAAAGACACCGACAACTTTCTT-ACAGCACCT-CTAACC-3'

Telorette3-NB02:
5'-P-TGCTCCGTGCATCTCC-AAGGTT-ACAGACGACTACAAACGGAATCGA-ACAGCACCT-CTAACC-3'

Telorette3-NB03:
5'-P-TGCTCCGTGCATCTCC-AAGGTT-CCTGGTAACTGGGACACAAGACTC-ACAGCACCT-CTAACC-3'

Teltail-tether: 5'-AACCTTGGAGATGCACGGAGCAAGCAAT-3'

Computational processing of Nanopore sequencing reads

Sequence base calling from the raw data was performed with the Nanopore *Guppy* application. Telomeric reads were processed computationally using the R package *Biostrings.*The scripts developed during this work for analyzing telomere reads are available on GitHub (x). FastQ files were read using the *readDNAStringSet* function and telomeric repeats identified with the *matchPattern* function searching for the repeat CCCTRR (at 6 permutations), where R is a

purine (A or G) since we noticed frequent errors reading G instead of A in the context of the telomeric repeats. The *union* function was used to combine the ranges of each pattern. The telomere length and read lengths were extracted and presented on plots of telomere density along the entire read. Telomere density was calculated in a moving window of 50 nucleotides and describes the portion within each 50 nucleotide sequence that contains telomeric repeats (1 is fully telomeric and 0, no telomeric repeats).

Liver repopulation study

A total of 200,000 hepatocytes (100,000 from each *Rtel1*$^{K/K}$ mutant and UBC-GFP mouse; Jackson Laboratory #004353) were injected into the spleen of the FAH mice after removal of NTBC water as described (Reizel et al., 2021). At the end of the study, livers were harvested for evaluation using immunostaining and quantified using *NIH ImageJ* (Rasband, 1997-2014).

Tissue Immunohistochemistry and Immunofluorescence

For EdU treatment, 150 μL of 10 mg/mL EdU solution was injected intraperitoneally two hours before mice were sacrificed. After euthanasia, mouse tissues were rinsed in PBS and fixed with 4% paraformaldehyde overnight. Fixed tissue was rinsed in PBS three times for 30 minutes per rinse and dehydrated for paraffin embedding and sectioning. EdU was detected according to the manufacturer's protocol (Click-iT Plus EdU Cell Proliferation Kit for Imaging, Alexa Fluor 647 dye, C10640, Invitrogen). Briefly, tissue sections were deparaffinized, and heat antigen retrieval was performed in a pressure cooker with Citrate Buffer, pH 6 (64142-07, Electron Microscopy Sciences). The tissue sections were then incubated in the Click-iT Edu Reaction Cocktail for 30 minutes at room temperature, washed, and blocked with CAS-Block (008120, Invitrogen) for 30 minutes at room temperature. Tissue sections were stained overnight with a mouse anti-E-

Cadherin (610181, 1:500, BD Biosciences) primary antibody. The following day, tissue sections were rinsed in PBS and incubated for two hours at room temperature with a Cy2 anti-mouse secondary antibody. The tissue sections were washed in PBS and stained with Hoechst (H3570, 1:10,000, Molecular Probes) to visualize nuclei. Images were taken on a Leica laser scanning confocal microscope (TCS SP8, Penn Cell & Developmental Biology Microscopy Core). Images were processed and brightness and contrast were enhanced using FIJI (ImageJ, Version 2.1.0, NIH) (Rasband, 1997-2014).

For FAH and GFP staining, slides were subjected to heat antigen retrieval in a pressure cooker with Bulls Eye Decloaking buffer (Biocare). Slides were incubated in primary antibody overnight and secondary antibody conjugated to peroxidase, and then developed using Tyramide Signal Amplification (TSA, Akoya Biosciences). Primary antibodies used for staining were: Rabbit anti-FAH (ThermoFisher; PA542049) and Goat anti-GFP (Abcam; AB6673). TSA-conjugated secondary antibodies (Cy2 and Cy3) were used. Images were taken using a Keyence All-in-One Fluorescence BZX800 microscope with brightfield capabilities. Animals were assigned to condition by genotype and were age-matched mice from the same colony

Data and code availability

Representative gels are shown in Figures 2, 5, S2-S4, S7 and S8. All measured and calculated values are provided in the Supplementary Tables 1 (MEFs) and 3 (mice). The complete un-spliced gel images for Figure 2A are shown in Figures S2A,C,E. The complete un-spliced gel images for Figure 5B, including the native hybridization, are shown in Figure S7D,H.

Additional gel replicates and data are available upon request to the corresponding authors. The telomeric read characteristics are summarized in Supplementary Table 2. The code used for filtering and processing Nanopore sequencing reads is available at GitHub.

Statistical analysis

Statistical analysis was performed by Microsoft Excel and GraphPad Prism 8.0, using simple linear and polynomial nonlinear regression, nested t-test, and two-tailed Student's t-test. $P < 0.05$ was considered statistically significant.

REFERENCES

Afonine, P.V., Mustyakimov, M., Grosse-Kunstleve, R.W., Moriarty, N.W., Langan, P., and Adams, P.D. (2010). Joint X-ray and neutron refinement with phenix.refine. Acta Crystallogr D Biol Crystallogr *66*, 1153-1163. 10.1107/S0907444910026582.

Al-Rahawan, M.M., Giri, N., and Alter, B.P. (2006). Intensive immunosuppression therapy for aplastic anemia associated with dyskeratosis congenita. Int J Hematol *83*, 275-276. 10.1532/IJH97.06030.

Armanios, M.Y., Chen, J.J., Cogan, J.D., Alder, J.K., Ingersoll, R.G., Markin, C., Lawson, W.E., Xie, M., Vulto, I., Phillips, J.A., 3rd, et al. (2007). Telomerase mutations in families with idiopathic pulmonary fibrosis. N Engl J Med *356*, 1317-1326. 10.1056/NEJMoa066157.

Awad, A., Glousker, G., Lamm, N., Tawil, S., Hourvitz, N., Smoom, R., Revy, P., and Tzfati, Y. (2020). Full length RTEL1 is required for the elongation of the single-stranded telomeric overhang by telomerase. Nucleic Acids Res *48*, 7239-7251. 10.1093/nar/gkaa503.

Ballew, B.J., Joseph, V., De, S., Sarek, G., Vannier, J.B., Stracker, T., Schrader, K.A., Small, T.N., O'Reilly, R., Manschreck, C., et al. (2013a). A recessive founder mutation in regulator of telomere elongation helicase 1, RTEL1, underlies severe immunodeficiency and features of Hoyeraal Hreidarsson syndrome. PLoS Genet *9*, e1003695. 10.1371/journal.pgen.1003695.

Ballew, B.J., Yeager, M., Jacobs, K., Giri, N., Boland, J., Burdett, L., Alter, B.P., and Savage, S.A. (2013b). Germline mutations of regulator of telomere elongation helicase 1, RTEL1, in Dyskeratosis congenita. Hum Genet *132*, 473-480. 10.1007/s00439-013-1265-8.

Blasco, M.A., Lee, H.W., Hande, M.P., Samper, E., Lansdorp, P.M., DePinho, R.A., and Greider, C.W. (1997). Telomere shortening and tumor formation by mouse cells lacking telomerase RNA. Cell *91*, 25-34.

Boyle, J.M., Hennick, K.M., Regalado, S.G., Vogan, J.M., Zhang, X., Collins, K., and Hockemeyer, D. (2020). Telomere length set point regulation in human pluripotent stem cells critically depends on the shelterin protein TPP1. Mol Biol Cell *31*, 2583-2596. 10.1091/mbc.E19-08-0447.

Chakravarti, D., LaBella, K.A., and DePinho, R.A. (2021). Telomeres: history, health, and hallmarks of aging. Cell *184*, 306-322. 10.1016/j.cell.2020.12.028.

Cheng, F., Luk, A.O., Shi, M., Huang, C., Jiang, G., Yang, A., Wu, H., Lim, C.K.P., Tam, C.H.T., Fan, B., et al. (2022). Shortened Leukocyte Telomere Length Is Associated With Glycemic Progression in Type 2 Diabetes: A Prospective and Mendelian Randomization Analysis. Diabetes Care *45*, 701-709. 10.2337/dc21-1609.

Cheng, K., and Wigley, D.B. (2018). DNA translocation mechanism of an XPD family helicase. Elife *7*. 10.7554/eLife.42400.

de Lange, T. (2018). Shelterin-Mediated Telomere Protection. Annu Rev Genet *52*, 223-247. 10.1146/annurev-genet-032918-021921.

Deng, Z., Glousker, G., Molczan, A., Fox, A.J., Lamm, N., Dheekollu, J., Weizman, O.E., Schertzer, M., Wang, Z., Vladimirova, O., et al. (2013). Inherited mutations in the helicase RTEL1 cause telomere dysfunction and Hoyeraal-Hreidarsson syndrome. Proc Natl Acad Sci U S A *110*, E3408-3416. 10.1073/pnas.1300600110.

Di Micco, R., Cicalese, A., Fumagalli, M., Dobreva, M., Verrecchia, A., Pelicci, P.G., and di Fagagna, F. (2008). DNA damage response activation in mouse embryonic fibroblasts undergoing replicative senescence and following spontaneous immortalization. Cell cycle (Georgetown, Tex *7*, 3601-3606. 10.4161/cc.7.22.7152.

Ding, H., Schertzer, M., Wu, X., Gertsenstein, M., Selig, S., Kammori, M., Pourvali, R., Poon, S., Vulto, I., Chavez, E., et al. (2004). Regulation of murine telomere length by Rtel: an essential gene encoding a helicase-like protein. Cell *117*, 873-886. 10.1016/j.cell.2004.05.026.

Duckworth, A., Gibbons, M.A., Allen, R.J., Almond, H., Beaumont, R.N., Wood, A.R., Lunnon, K., Lindsay, M.A., Wain, L.V., Tyrrell, J., and Scotton, C.J. (2021). Telomere length and risk of idiopathic pulmonary fibrosis and chronic obstructive pulmonary disease: a mendelian randomisation study. Lancet Respir Med *9*, 285-294. 10.1016/S2213-2600(20)30364-7.

Ghisays, F., Garzia, A., Wang, H., Canasto-Chibuque, C., Hohl, M., Savage, S.A., Tuschl, T., and Petrini, J.H.J. (2021). RTEL1 influences the abundance and localization of TERRA RNA. Nat Commun *12*, 3016. 10.1038/s41467-021-23299-2.

Glousker, G., Touzot, F., Revy, P., Tzfati, Y., and Savage, S.A. (2015). Unraveling the pathogenesis of Hoyeraal-Hreidarsson syndrome, a complex telomere biology disorder. British journal of haematology *170*, 457-471. 10.1111/bjh.13442.

Gohring, J., Fulcher, N., Jacak, J., and Riha, K. (2014). TeloTool: a new tool for telomere length measurement from terminal restriction fragment analysis with improved probe intensity correction. Nucleic Acids Res *42*, e21. 10.1093/nar/gkt1315.

Grill, S., and Nandakumar, J. (2021). Molecular mechanisms of telomere biology disorders. J Biol Chem *296*, 100064. 10.1074/jbc.REV120.014017.

Grompe, M. (2017). Fah Knockout Animals as Models for Therapeutic Liver Repopulation. Adv Exp Med Biol *959*, 215-230. 10.1007/978-3-319-55780-9_20.

Hanahan, D. (2022). Hallmarks of Cancer: New Dimensions. Cancer Discov *12*, 31-46. 10.1158/2159-8290.CD-21-1059.

Hemann, M.T., Strong, M.A., Hao, L.Y., and Greider, C.W. (2001). The shortest telomere, not average telomere length, is critical for cell viability and chromosome stability. Cell *107*, 67-77.

Kelley, L.A., Mezulis, S., Yates, C.M., Wass, M.N., and Sternberg, M.J. (2015). The Phyre2 web portal for protein modeling, prediction and analysis. Nature protocols *10*, 845-858. 10.1038/nprot.2015.053.

Kim, S.H., Parrinello, S., Kim, J., and Campisi, J. (2003). Mus musculus and Mus spretus homologues of the human telomere-associated protein TIN2. Genomics *81*, 422-432. 10.1016/s0888-7543(02)00033-2.

Kirwan, M., Vulliamy, T., Marrone, A., Walne, A.J., Beswick, R., Hillmen, P., Kelly, R., Stewart, A., Bowen, D., Schonland, S.O., et al. (2009). Defining the pathogenic role of telomerase mutations in myelodysplastic syndrome and acute myeloid leukemia. Hum Mutat *30*, 1567-1573. 10.1002/humu.21115.

Kotsantis, P., Segura-Bayona, S., Margalef, P., Marzec, P., Ruis, P., Hewitt, G., Bellelli, R., Patel, H., Goldstone, R., Poetsch, A.R., and Boulton, S.J. (2020). RTEL1 Regulates G4/R-Loops to Avert Replication-Transcription Collisions. Cell reports *33*, 108546. 10.1016/j.celrep.2020.108546.

Lamm, N., Ordan, E., Shponkin, R., Richler, C., Aker, M., and Tzfati, Y. (2009). Diminished telomeric 3' overhangs are associated with telomere dysfunction in Hoyeraal-Hreidarsson syndrome. PLoS One *4*, e5666. 10.1371/journal.pone.0005666.

Lansdorp, P., and van Wietmarschen, N. (2019). Helicases FANCJ, RTEL1 and BLM Act on Guanine Quadruplex DNA in Vivo. Genes (Basel) *10*. 10.3390/genes10110870.

Lansdorp, P.M. (2022). Telomeres, aging, and cancer: the big picture. Blood *139*, 813-821. 10.1182/blood.2021014299.

Le Guen, T., Jullien, L., Touzot, F., Schertzer, M., Gaillard, L., Perderiset, M., Carpentier, W., Nitschke, P., Picard, C., Couillault, G., et al. (2013). Human RTEL1 deficiency causes Hoyeraal-Hreidarsson syndrome with short telomeres and genome instability. Hum Mol Genet *22*, 3239-3249. 10.1093/hmg/ddt178.

Lee, H.W., Blasco, M.A., Gottlieb, G.J., Horner, J.W., 2nd, Greider, C.W., and DePinho, R.A. (1998). Essential role of mouse telomerase in highly proliferative organs. Nature *392*, 569-574. 10.1038/33345.

Li, H., Wei, C., Zhou, R., Wang, B., Zhang, Y., Shao, C., and Luo, Y. (2019). Mouse models in modeling aging and cancer. Exp Gerontol *120*, 88-94. 10.1016/j.exger.2019.03.002.

LLC, S. The PyMOL Molecular Graphics System

Maciejowski, J., and de Lange, T. (2017). Telomeres in cancer: tumour suppression and genome instability. Nat Rev Mol Cell Biol *18*, 175-186. 10.1038/nrm.2016.171.

Nassour, J., Schmidt, T.T., and Karlseder, J. (2021). Telomeres and Cancer: Resolving the Paradox. Annu Rev Cancer Biol *5*, 59-77. 10.1146/annurev-cancerbio-050420-023410.

Pettersen, E.F., Goddard, T.D., Huang, C.C., Couch, G.S., Greenblatt, D.M., Meng, E.C., and Ferrin, T.E. (2004). UCSF Chimera--a visualization system for exploratory research and analysis. J Comput Chem *25*, 1605-1612. 10.1002/jcc.20084.

Porreca, R.M., Glousker, G., Awad, A., Matilla Fernandez, M.I., Gibaud, A., Naucke, C., Cohen, S.B., Bryan, T.M., Tzfati, Y., Draskovic, I., and Londono-Vallejo, A. (2018). Human RTEL1 stabilizes long G-overhangs allowing telomerase-dependent over-extension. Nucleic Acids Res *46*, 4533-4545. 10.1093/nar/gky173.

Prowse, K.R., and Greider, C.W. (1995). Developmental and tissue-specific regulation of mouse telomerase and telomere length. Proc Natl Acad Sci U S A *92*, 4818-4822.

Rasband, W.S. (1997-2014). ImageJ.

Reizel, Y., Morgan, A., Gao, L., Schug, J., Mukherjee, S., Garcia, M.F., Donahue, G., Baur, J.A., Zaret, K.S., and Kaestner, K.H. (2021). FoxA-dependent demethylation of DNA initiates epigenetic memory of cellular identity. Dev Cell *56*, 602-612 e604. 10.1016/j.devcel.2021.02.005.

Roake, C.M., and Artandi, S.E. (2020). Regulation of human telomerase in homeostasis and disease. Nat Rev Mol Cell Biol *21*, 384-397. 10.1038/s41580-020-0234-z.

Rossiello, F., Jurk, D., Passos, J.F., and d'Adda di Fagagna, F. (2022). Telomere dysfunction in ageing and age-related diseases. Nat Cell Biol *24*, 135-147. 10.1038/s41556-022-00842-x.

Schertzer, M., Jouravleva, K., Perderiset, M., Dingli, F., Loew, D., Le Guen, T., Bardoni, B., de Villartay, J.P., Revy, P., and Londono-Vallejo, A. (2015). Human regulator of telomere elongation helicase 1 (RTEL1) is required for the nuclear and cytoplasmic trafficking of pre-U2 RNA. Nucleic Acids Res *43*, 1834-1847. 10.1093/nar/gku1402.

Schilbach, S., Aibara, S., Dienemann, C., Grabbe, F., and Cramer, P. (2021). Structure of RNA polymerase II pre-initiation complex at 2.9 A defines initial DNA opening. Cell *184*, 4064-4072 e4028. 10.1016/j.cell.2021.05.012.

Sfeir, A.J., Chai, W., Shay, J.W., and Wright, W.E. (2005). Telomere-end processing the terminal nucleotides of human chromosomes. Mol Cell *18*, 131-138. 10.1016/j.molcel.2005.02.035.

Tyson, J. (2020). Bead-free long fragment LSK109 library preparation. Protocols.io. https://dx.doi.org/10.17504/protocols.io.7eshjee.

Uringa, E.J., Lisaingo, K., Pickett, H.A., Brind'amour, J., Rohde, J.H., Zelensky, A., Essers, J., and Lansdorp, P.M. (2012). RTEL1 contributes to DNA replication and repair and telomere maintenance. Mol Biol Cell *23*, 2782-2792. 10.1091/mbc.E12-03-0179.

van Batenburg, A.A., Kazemier, K.M., Peeters, T., van Oosterhout, M.F.M., van der Vis, J.J., Grutters, J.C., Goldschmeding, R., and van Moorsel, C.H.M. (2018). Cell Type-Specific Quantification of Telomere Length and DNA Double-strand Breaks in Individual Lung Cells by Fluorescence In Situ Hybridization and Fluorescent Immunohistochemistry. J Histochem Cytochem *66*, 485-495. 10.1369/0022155418761351.

van der Lelij, P., Chrzanowska, K.H., Godthelp, B.C., Rooimans, M.A., Oostra, A.B., Stumm, M., Zdzienicka, M.Z., Joenje, H., and de Winter, J.P. (2010). Warsaw breakage syndrome, a cohesinopathy associated with mutations in the XPD helicase family member DDX11/ChlR1. Am J Hum Genet *86*, 262-266. S0002-9297(10)00009-1 [pii]

10.1016/j.ajhg.2010.01.008.

Vannier, J.B., Pavicic-Kaltenbrunner, V., Petalcorin, M.I., Ding, H., and Boulton, S.J. (2012). RTEL1 Dismantles T Loops and Counteracts Telomeric G4-DNA to Maintain Telomere Integrity. Cell *149*, 795-806. 10.1016/j.cell.2012.03.030.

Vannier, J.B., Sandhu, S., Petalcorin, M.I., Wu, X., Nabi, Z., Ding, H., and Boulton, S.J. (2013). RTEL1 is a replisome-associated helicase that promotes telomere and genome-wide replication. Science *342*, 239-242. 10.1126/science.1241779.

Vaziri, H., and Benchimol, S. (1998). Reconstitution of telomerase activity in normal human cells leads to elongation of telomeres and extended replicative life span. Curr Biol *8*, 279-282.

Walne, A.J., Vulliamy, T., Kirwan, M., Plagnol, V., and Dokal, I. (2013). Constitutional mutations in RTEL1 cause severe dyskeratosis congenita. Am J Hum Genet *92*, 448-453. 10.1016/j.ajhg.2013.02.001.

Wu, W., Bhowmick, R., Vogel, I., Ozer, O., Ghisays, F., Thakur, R.S., Sanchez de Leon, E., Richter, P.H., Ren, L., Petrini, J.H., et al. (2020). RTEL1 suppresses G-quadruplex-associated R-loops at difficult-to-replicate loci in the human genome. Nat Struct Mol Biol *27*, 424-437. 10.1038/s41594-020-0408-6.

Wu, Y., Suhasini, A.N., and Brosh, R.M., Jr. (2009). Welcome the family of FANCJ-like helicases to the block of genome stability maintenance proteins. Cell Mol Life Sci *66*, 1209-1222. 10.1007/s00018-008-8580-6.

Yang, H., Wang, H., and Jaenisch, R. (2014). Generating genetically modified mice using CRISPR/Cas-mediated genome engineering. Nature protocols *9*, 1956-1968. 10.1038/nprot.2014.134.

Zhu, L., Hathcock, K.S., Hande, P., Lansdorp, P.M., Seldin, M.F., and Hodes, R.J. (1998). Telomere length regulation in mice is linked to a novel chromosome locus. Proc Natl Acad Sci U S A *95*, 8648-8653.

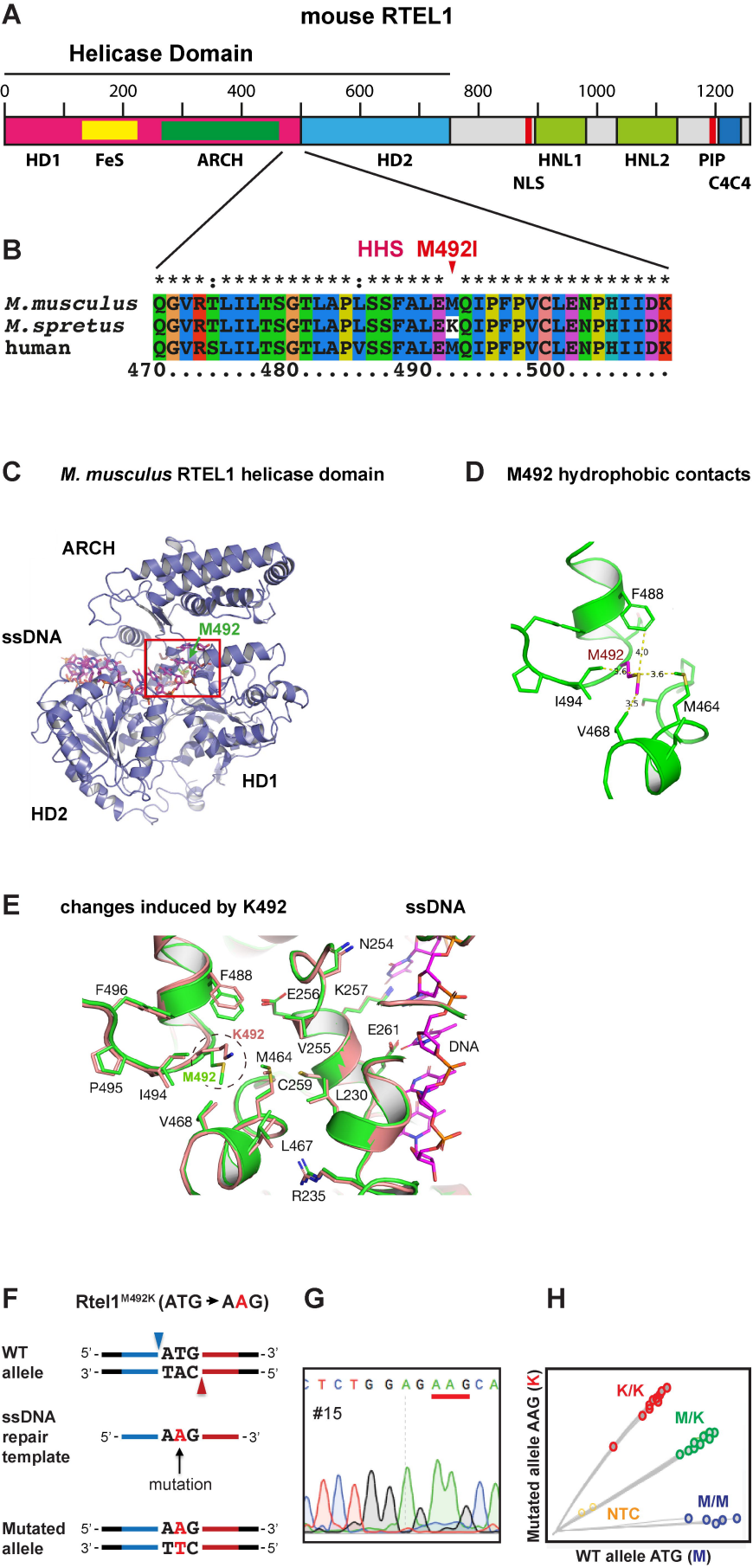
A
mouse RTEL1
Helicase Domain
0
200
400
600
800
1000
1200
HD1
FeS
ARCH
HD2
HNL1
HNL2
PIP
NLS
C4C4
B
HHS M492I
M.musculus
M.spretus
human
470.....480.....490.....500.....
C
M. musculus RTEL1 helicase domain
ARCH
ssDNA
M492
HD1
HD2
D
M492 hydrophobic contacts
F488
M492
I494
M464
V468
E
changes induced by K492
ssDNA
N254
F488
F496
E256
K257
K492
E261
V255
DNA
M464
M492
P495
I494
C259
L230
V468
L467
R235
F
Rtel1M492K (ATG→AAG)
WT allele
5'- ATG -3'
3'- TAC -5'
ssDNA repair template
5'- AAG -3'
mutation
Mutated allele
5'- AAG -3'
3'- TTC -5'
G
#15
H
K/K
M/K
M/M
NTC
Mutated allele AAG (K)
WT allele ATG (M)

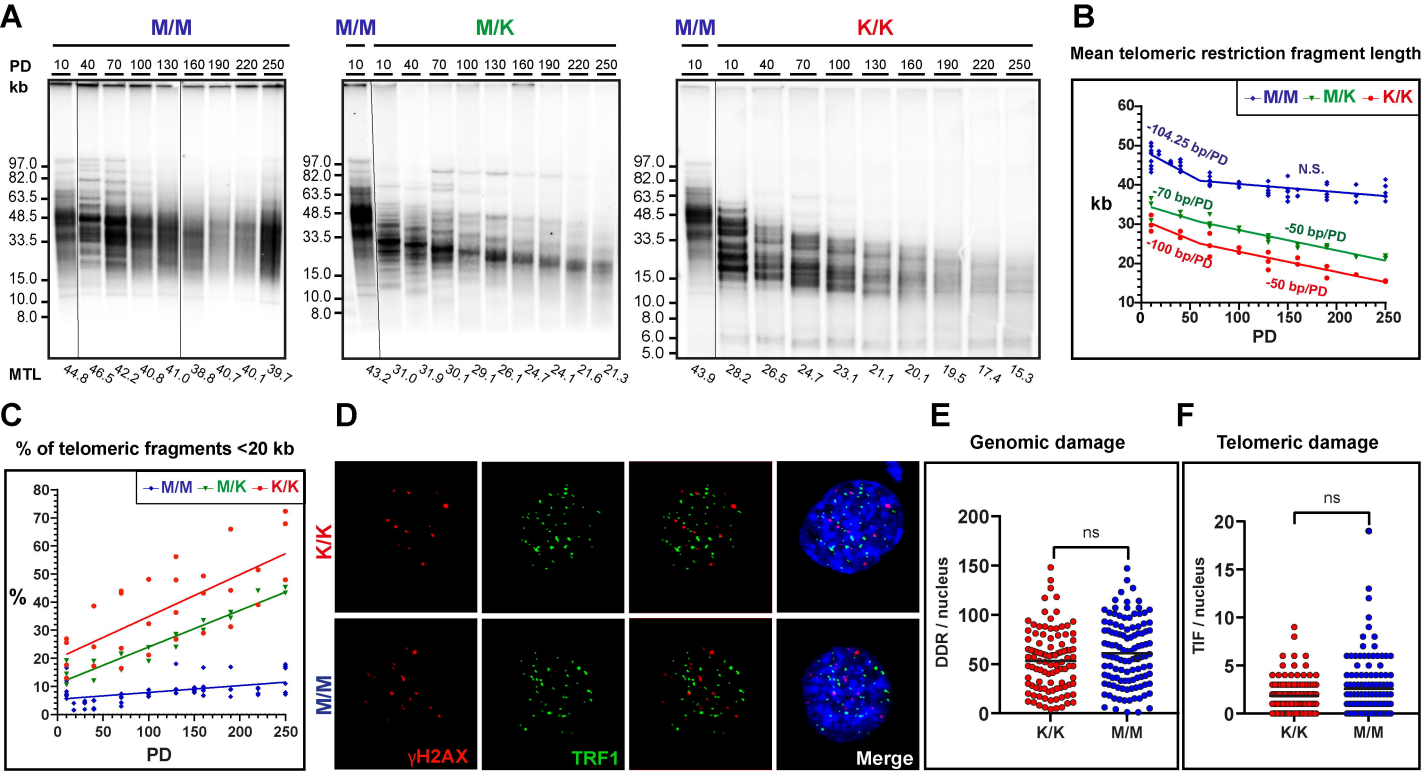
A
M/M
PD
10 40 70 100 130 160 190 220 250
kb
97.0
82.0
63.5
48.5
33.5
15.0
10.0
8.0
MTL
44.8 46.5 42.2 40.8 41.0 38.8 40.7 40.1 39.7
M/M
M/K
10 10 40 70 100 130 160 190 220 250
97.0
82.0
63.5
48.5
33.5
15.0
10.0
8.0
43.2 31.0 31.9 30.1 29.1 26.1 24.7 24.1 21.6 21.3
M/M
K/K
10 10 40 70 100 130 160 190 220 250
97.0
82.0
63.5
48.5
33.5
15.0
10.0
8.0
6.0
5.0
43.9 28.2 26.5 24.7 23.1 21.1 20.1 19.5 17.4 15.3
B
Mean telomeric restriction fragment length
M/M
M/K
K/K
kb
PD
-104.25 bp/PD
N.S.
-70 bp/PD
-50 bp/PD
-100 bp/PD
-50 bp/PD
C
% of telomeric fragments <20 kb
M/M
M/K
K/K
%
PD
D
K/K
M/M
γH2AX
TRF1
Merge
E
Genomic damage
DDR / nucleus
ns
K/K
M/M
F
Telomeric damage
TIF / nucleus
ns
K/K
M/M

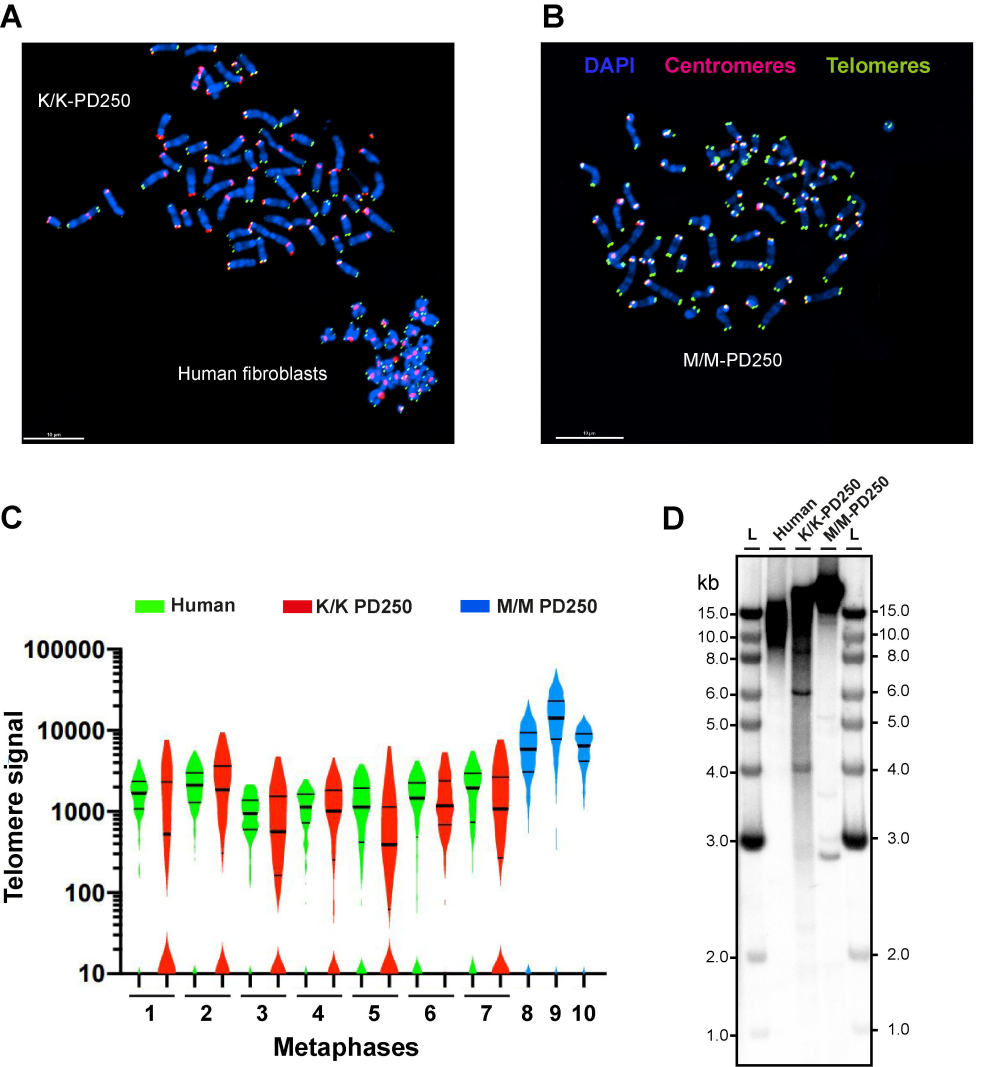
A
K/K-PD250
Human fibroblasts
B
DAPI
Centromeres
Telomeres
M/M-PD250
C
Human
K/K PD250
M/M PD250
Telomere signal
100000
10000
1000
100
10
1
2
3
4
5
6
7
8
9
10
Metaphases
D
L
Human
K/K-PD250
M/M-PD250
L
kb
15.0
10.0
8.0
6.0
5.0
4.0
3.0
2.0
1.0

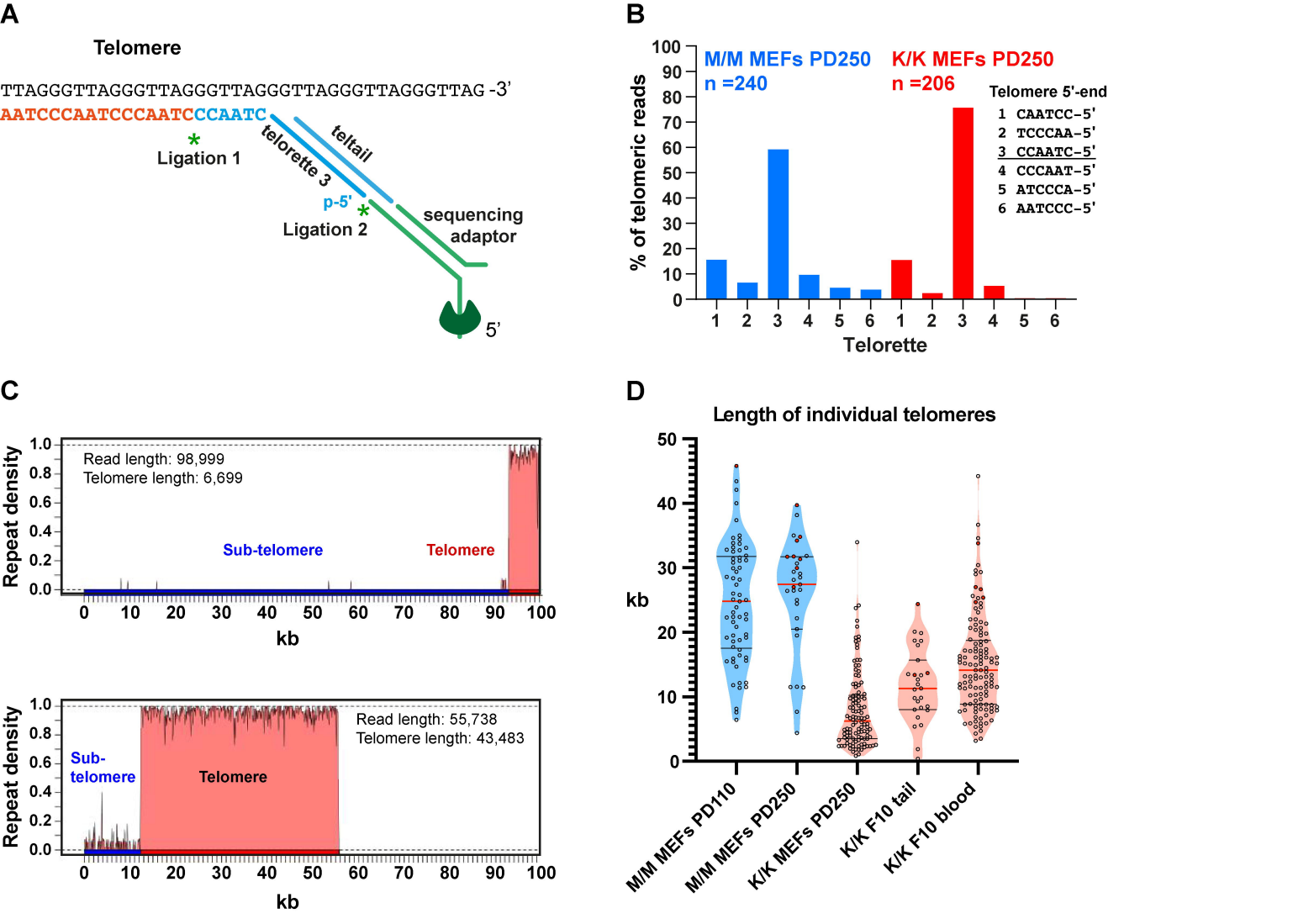
A
Telomere
TTAGGGTTAGGGTTAGGGTTAGGGTTAGGGTTAGGGTTAG -3'
AATCCCAATCCCAATCCCAATC
Ligation 1
telorette 3
teltail
p-5'
Ligation 2
sequencing adaptor
5'
B
M/M MEFs PD250
n =240
K/K MEFs PD250
n =206
Telomere 5'-end
1 CAATCC-5'
2 TCCCAA-5'
3 CCAATC-5'
4 CCCAAT-5'
5 ATCCCA-5'
6 AATCCC-5'
% of telomeric reads
Telorette
C
Read length: 98,999
Telomere length: 6,699
Sub-telomere
Telomere
Repeat density
kb
Read length: 55,738
Telomere length: 43,483
Sub-telomere
Telomere
Repeat density
kb
D
Length of individual telomeres
kb
M/M MEFs PD110
M/M MEFs PD250
K/K MEFs PD250
K/K F10 tail
K/K F10 blood

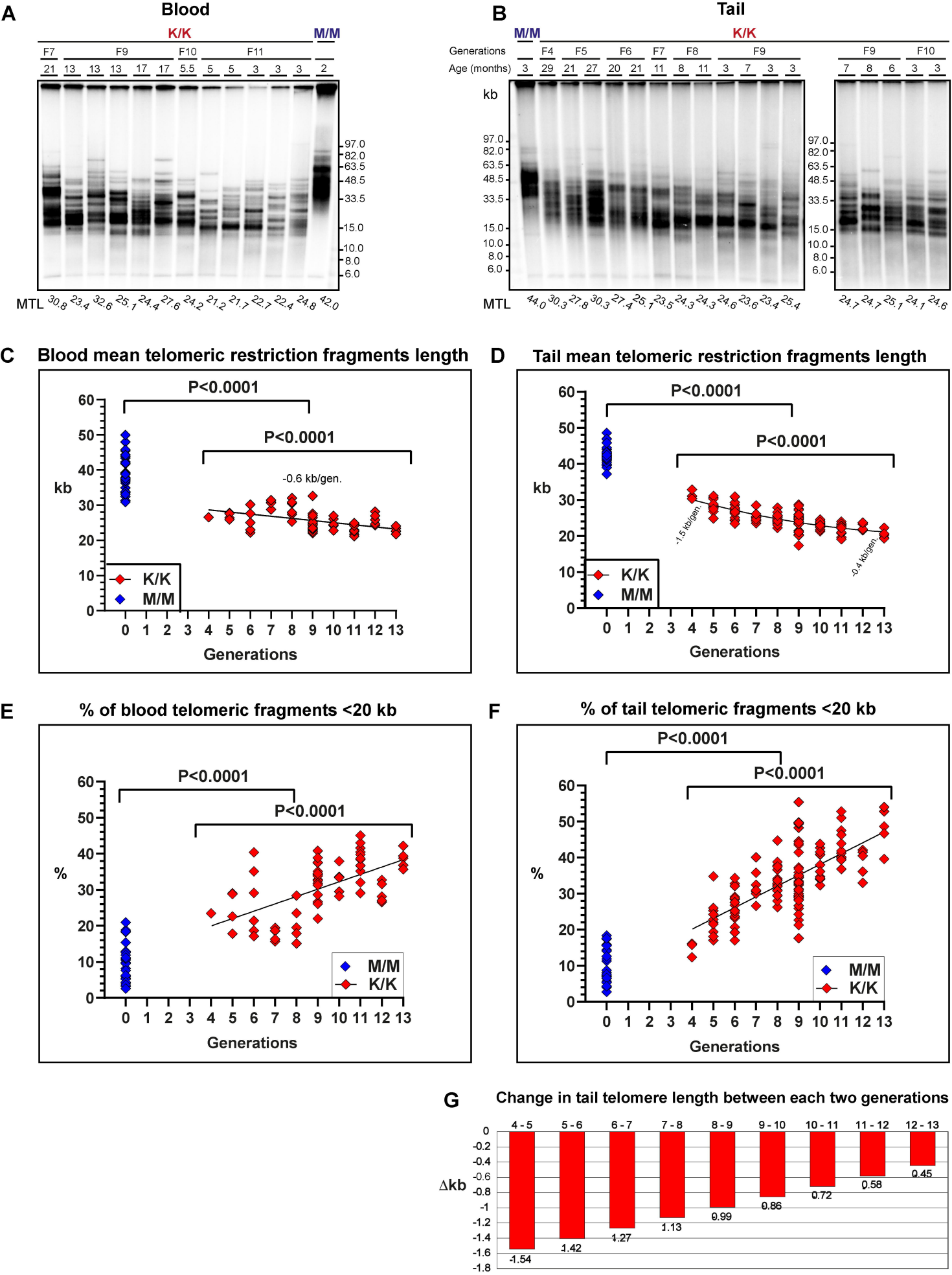
A
Blood
K/K
M/M
F7
F9
F10
F11
21 13 13 13 17 17 5.5 5 5 3 3 3 2
97.0
82.0
63.5
48.5
33.5
15.0
10.0
8.0
6.0
MTL 30.8 23.4 32.6 25.1 24.4 27.6 24.2 21.2 21.7 22.7 22.4 24.8 42.0
B
Tail
M/M
K/K
Generations
F4 F5 F6 F7 F8 F9
F9 F10
Age (months)
3 29 21 27 20 21 11 8 11 3 7 3 3
7 8 6 3 3
kb
97.0
82.0
63.5
48.5
33.5
15.0
10.0
8.0
6.0
MTL 44.0 30.3 27.8 30.3 27.4 25.1 23.5 24.3 24.3 24.6 23.6 23.4 25.4
24.7 24.7 25.1 24.1 24.6
C
Blood mean telomeric restriction fragments length
P<0.0001
P<0.0001
-0.6 kb/gen.
kb
K/K
M/M
Generations
D
Tail mean telomeric restriction fragments length
P<0.0001
P<0.0001
-1.5 kb/gen.
-0.4 kb/gen.
kb
K/K
M/M
Generations
E
% of blood telomeric fragments <20 kb
P<0.0001
P<0.0001
%
M/M
K/K
Generations
F
% of tail telomeric fragments <20 kb
P<0.0001
P<0.0001
%
M/M
K/K
Generations
G
Change in tail telomere length between each two generations
4 - 5
5 - 6
6 - 7
7 - 8
8 - 9
9 - 10
10 - 11
11 - 12
12 - 13
Δkb
-1.54
-1.42
-1.27
-1.13
-0.99
-0.86
-0.72
-0.58
-0.45

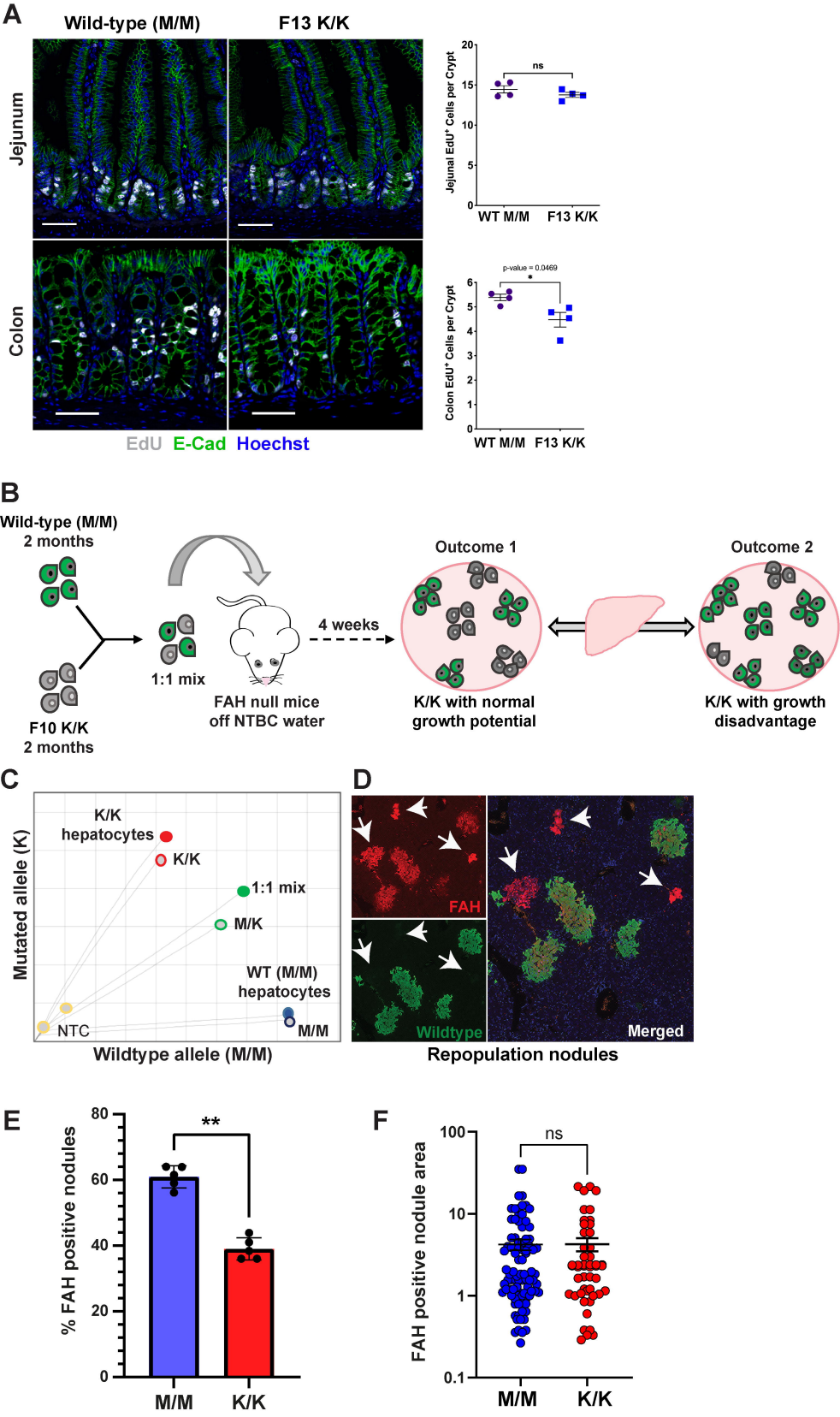
A
Wild-type (M/M)
F13 K/K
Jejunum
Colon
EdU E-Cad Hoechst
Jejunal EdU+ Cells per Crypt
ns
WT M/M
F13 K/K
Colon EdU+ Cells per Crypt
p-value = 0.0469
*
B
Wild-type (M/M)
2 months
F10 K/K
2 months
1:1 mix
FAH null mice
off NTBC water
4 weeks
Outcome 1
K/K with normal
growth potential
Outcome 2
K/K with growth
disadvantage
C
Mutated allele (K)
K/K
hepatocytes
K/K
1:1 mix
M/K
WT (M/M)
hepatocytes
NTC
M/M
Wildtype allele (M/M)
D
FAH
Wildtype
Merged
Repopulation nodules
E
% FAH positive nodules
**
M/M
K/K
F
FAH positive nodule area
ns
M/M
K/K